J. Plasma Physics (2015), *vol.* 81, 345810104 © Cambridge University Press 2014
doi:10.1017/S0022377814000919

The HelCat basic plasma science device

M. Gilmore[1]†, A. G. Lynn[1], T. R. Desjardins[1], Y. Zhang[1], C. Watts[1,2], S. C. Hsu[3], S. Betts[1], R. Kelly[1] and E. Schamiloglu[1]

[1]Department of Electrical and Computer Engineering, University of New Mexico, Albuquerque, NM 87131, USA
[2]ITER Organization, St. Paul-lès-Durance, France
[3]Los Alamos National Laboratory, Los Alamos, NM 87545, USA

(Received 31 July 2014; revised 12 September 2014; accepted 26 September 2014; first published online 14 November 2014)

The Helicon-Cathode(HelCat) device is a medium-size linear experiment suitable for a wide range of basic plasma science experiments in areas such as electrostatic turbulence and transport, magnetic relaxation, and high power microwave (HPM)-plasma interactions. The HelCat device is based on dual plasma sources located at opposite ends of the 4 m long vacuum chamber – an RF helicon source at one end and a thermionic cathode at the other. Thirteen coils provide an axial magnetic field $B \leqslant 0.220$ T that can be configured individually to give various magnetic configurations (e.g. solenoid, mirror, cusp). Additional plasma sources, such as a compact coaxial plasma gun, are also utilized in some experiments, and can be located either along the chamber for perpendicular (to the background magnetic field) plasma injection, or at one of the ends for parallel injection. Using the multiple plasma sources, a wide range of plasma parameters can be obtained. Here, the HelCat device is described in detail and some examples of results from previous and ongoing experiments are given. Additionally, examples of planned experiments and device modifications are also discussed.

1. Introduction

Large user facilities play an important role in science, including basic plasma science, by being able to push physics parameters to the state of the art, to draw on relatively large facility and staff infrastructure, and by serving a large community of users. However, such large facilities can also be limited in their range of accessible physics parameter space, their ability to dynamically make changes to device configurations demanded by some experiments, and in run time available to an individual user. Thus, 'medium-scale' devices also fill an import niche in basic science. By 'medium-scale' we mean devices that are large enough so that the physics to be studied is not seriously limited (in physical size, power, diagnostics, etc.), but that can be easily reconfigured to suit a given experiment. The LAPD-U (Leneman et al. 2006) and the TORPEX (Fasoli et al. 2006) devices are examples of large and medium scale basic plasma science experiments, respectively. The HelCat (Helicon-Cathode) basic plasma science device at the University of New Mexico (UNM) was built to help fill this 'medium-scale' experiment niche.

† Email address for correspondence: mgilmore@unm.edu

https://doi.org/10.1017/S0022377814000919 Published online by Cambridge University Press

HelCat is built around two plasma sources located at either end of the experiment – an RF helicon source and a thermionic cathode source. These two sources, plus an additional plasma gun source, allow a wide range of plasma parameters to be obtained, beyond what is possible with a single source. Magnet coils produce an axial B-field up to 0.22 T. The three sources can be operated independently or simultaneously.

The helicon source can be operated in either inductively coupled mode or helicon mode, depending on RF power to the antenna, which can give peak densities from $n_{peak} \sim 10^{16} - 10^{20}$ m^{-3}, with near-Gaussian radial density profiles of full width, half maximum (FWHM) typically ~6.5 cm. Plasma density profiles are measured using a scanned Langmuir probe collecting ion saturation current normalized using one of the interferometers (40 or 94 GHz depending on the density range). Low power inductive and helicon plasmas (e.g. $P_{RF} < 1$ kW) are quiescent, while higher power helicon discharges exhibit 'intrinsic' edge fluctuations, which can be coherent or turbulent, depending on parameters. Cathode plasmas typically have peak densities n_{peak} ~0.7–7 $\times 10^{18}$ m^{-3}, with radial density profiles varying from strongly peaked to flat with steep edge gradients ($L_n = ((1/n)dn/dr)^{-1} \sim$ 1–20 cm) and FWHM ~7.5 cm. Ion temperature is not measured in HelCat for either of these sources, but similar helicon devices have reported T_i ~0.1–0.75 eV (Scime et al. 2013) and similar cathode devices have reported $T_i \sim 1$ eV (Leneman et al. 2006). Other relevant plasma parameters are given in Table 1. Parameters in Table 1 use standard variable names, which are defined in Appendix A.

Other plasma sources have also operated on HelCat. For example, a compact coaxial plasma gun has been constructed (Zhang et al. 2009) and can be mounted on the chamber end or side. The gun is fitted with its own solenoidal field coil, which produces an axial bias B-field in the gun up to ~1 T. This gun is capable of producing jet-like (open field line) or spheromak-like (closed field line) plasmas with trapped magnetic field $B \sim 0.01$ T, depending on operating parameters. Plasma velocities are sonic to 2 – 3 times supersonic, also depending on parameters. Typical gun plasmas have $n \sim 10^{20}$ m^{-3}, $T_e \sim 5 - 10$ eV, and $T_i \sim 10 - 15$ eV.

Each of the sources mentioned above is capable of operating with various fill gases, including Ar, Ne, He, and H (cathode and gun only). In addition to the plasma parameters given in the first table, Table 2 gives ranges of some relevant scaled physics parameters for Ar and He for helicon, cathode, and compact gun plasmas.

2. HelCat device description

The HelCat device, shown in Fig. 1, has been described in detail previously (Lynn et al. 2009), and will be only briefly described here. The plasma gun system is described in Sec. 3.2. HelCat is built around a 4 m long, 50 cm inside diameter stainless steel vacuum chamber. Twenty 10 inch (25 cm), twenty-four 8 inch (20 cm), and twenty-eight 3.75 inch (9.5 cm) conflat flanges provide excellent port access to the device. An RF helicon source, consisting of a helical antenna placed outside of 40 cm long, 15 cm diameter Pyrex tube mounted on the stainless steel end flange, resides on the south end of the chamber. A three-stage amplifier provides up to 5 kW steady state or pulsed power to the antenna network, over 2–30 MHz. Typical operation is at 10 MHz. Both $m = 0$ and $m = 1$ helicon antennas have been operated (Light and Chen 1995), with the $m = 0$ producing a somewhat lower peak density, larger diameter plasma column. The physics of helicon discharges are complicated and will not be reviewed here. See (Chen and Arnush 1997) and references therein

https://doi.org/10.1017/S0022377814000919 Published online by Cambridge University Press

https://doi.org/10.1017/S0022377814000919 Published online by Cambridge University Press

	n_e (m^{-3})	T_e (eV)	Gas fill pressure (Pa)	λ_D (m)	ω_{ci} (rad/s)	ω_{ce} (rad/s)	ν_{ii} (s^{-1})	ν_{in} (s^{-1})	C_s (m/s)	V_A (m/s)
Argon										
Helicon	10^{16}–10^{20}	3–5	0.027–1.33	(4–40) $\times10^{-6}$	(1–50) $\times10^{4}$	(2–40) $\times10^{9}$	(0.3–400) $\times10^{6}$	(1–7) $\times10^{4}$	(2–4) $\times10^{3}$	(1–25) $\times10^{4}$
Cathode	(0.7–7) $\times10^{18}$	5–10	0.013–1.33	(10–100) $\times10^{-6}$	(1–50) $\times10^{4}$	(2–40) $\times10^{9}$	(1–400) $\times10^{7}$	(3–30) $\times10^{3}$	(3–5) $\times10^{3}$	(1–50) $\times10^{4}$
Gun	$\sim10^{20}$	5–10	$\sim$13 (puff)	(1–3) $\times10^{-6}$	(2–200) $\times10^{4}$	(2–180) $\times10^{9}$	$\sim5\times10^{5}$	(1–3) $\times10^{4}$	$\sim7\times10^{3}$	(3–400) $\times10^{3}$
Helium										
Helicon	10^{16}–10^{20}	3–5	0.027–1.33	(4–40) $\times10^{-6}$	(1–50) $\times10^{5}$	(2–40) $\times10^{9}$	(2–200) $\times10^{5}$	(1–10) $\times10^{4}$	(5–10) $\times10^{3}$	(3–75) $\times10^{4}$
Cathode	(0.7–7) $\times10^{18}$	5–10	0.013–1.33	(10–100) $\times10^{-6}$	(1–50) $\times10^{5}$	(2–40) $\times10^{9}$	(1–10) $\times10^{6}$	(3–30) $\times10^{3}$	(10–15) $\times10^{3}$	(4–100) $\times10^{4}$
Gun	$\sim10^{20}$	5–10	$\sim$13 (puff)	(1–3) $\times10^{-6}$	(2–200) $\times10^{5}$	(2–180) $\times10^{9}$	$\sim6\times10^{5}$	(1–3) $\times10^{5}$	$\sim2\times10^{4}$	(1–100) $\times10^{4}$

TABLE 1. Approximate HelCat plasma parameters.

	β	L_{nr} (cm)	a/ρ_i	a/ρ_s	ω_{ci}/ν_{in}	a/λ_{ii}	a/λ_{in}	a/λ_{ie}
Argon								
Helicon	$10^{-4}-0.1$	3–10	3–75	1–20	1–20	10–600	2–20	0.03–3
Cathode	$10^{-4}-0.1$	1–10	3–100	0.5–15	30–700	100–300	0.1–1	0.1–1
Gun	$10^{-4}-1$	~5	10–1000	10–1000	1–20	10–30	5–10	30–50
Helium								
Helicon	$10^{-4}-0.1$	3–10	10–250	3–60	3–70	$(6–200)\times10^3$	4–40	0.1–10
Cathode	$10^{-4}-0.1$	1–10	10–250	1–40	100–2000	100–400	0.1–1	0.1–1
Gun	$10^{-4}-1$	~5	10–1000	10–1000	2–50	10–30	5–10	30–50

TABLE 2. Approximate HelCat scaled parameters.

for detailed discussions. Typical HelCat helicon density, n, and electron temperature, T_e, radial profiles using an $m = 1$ antenna in Ar are shown in Fig. 2.

A Ni-BaO thermionic cathode, modeled after the large plasma device (LAPD) at UCLA (Gekelman et al. 1991), resides at the north chamber end. The cathode is a barium-strontium-calcium oxide coated nickel plate, radiantly heated from behind to ~900°C by a set of tungsten filaments heated by ~5 kW of DC current. The coated electron-emitting area is 15 cm in diameter. A copper mesh anode resides ~10 cm in front of the cathode, and a pulsed anode-cathode voltage is applied, typically ~50 V for ~10 ms. Electron discharge (emission) currents up to 600 A ($\leqslant 3$ A/cm^2) collisionally ionize the gas. Typical n and T_e profiles in Ar are shown in Fig. 3. The cathode/anode/heater assembly is mounted on a cart that can be retracted from the chamber end, allowing other structures or diagnostics to be mounted on the chamber north end.

Thirteen water-cooled magnet coils, able to operate steady state, surround the vacuum chamber, and can be individually powered so as to produce various magnetic field configurations, including solenoid, mirror, and cusp fields. For solenoidal fields, ripple is <1% on axis, and ~3% at the plasma edge at $R = 20$ cm. Two 1000 L/min turbomolecular pumps provide a base vacuum pressure $< 2.7 \times 10^{-5}$ Pa, and can be throttled for plasma operations at up to ~13 Pa. Typically, continuous gas feed/continuous pumping is utilized, except in the case of the coaxial gun source, where fast gas puffing is used. For continuous gas feed, constant pressure is maintained via a piezoelectric valve and feedback pressure controller with a 2 ms response time. The gas feed has been introduced at various positions along the chamber, for example in the middle, near the source end, or at the end opposite from the source. Little or no difference in gas pressure or plasma behavior has been observed with changing gas feed position.

Passive spectroscopic measurements indicate that that the neutral gas radial profile, $n_n(r)$, is hollow in helicon discharges, i.e. lower neutral density in the center than at the edge. An example is shown in Fig. 4, which plots $I_{ArI}/\sqrt{I_{ArII}}$ versus radius, measured by a survey spectrometer collecting radially-localized light via a fiber optic bundle and collimating lens viewing from the chamber end. Here, I_{ArI} and I_{ArII} are the intensity of ArI and ArII spectral lines, respectively. The measurement is axially-averaged over the machine length, but radially localized to ~3 cm. As discussed by Okamoto et al., $I_{ArI}/\sqrt{I_{ArII}}$ is proportional to n_n, so Fig. 4 gives an indication of the neutral density profile (Okamoto et al. 2003). Watts and Hanna have also predicted a hollow neutral radial profile in an identical helicon plasma based on a neutral diffusion model

https://doi.org/10.1017/S0022377814000919 Published online by Cambridge University Press

(Watts and Hanna 2004). A neutral Ar laser induced fluorescence (LIF) system is currently in development to better quantify neutral density, temperature and flow velocity.

A rectangular vacuum 'box port' of inside dimension 65 cm W × 108 cm H, shown in Fig. 5, is located between the 4 m chamber and the south end flange on which the helicon source is mounted. This allows structures, such as grid (mesh) electrodes, as large as the entire chamber diameter (50 cm) to be inserted in front of the helicon source. A large rectangular window, 20 × 40 cm, also shown in Fig. 5, mounted on a 50 cm ISO end flange can be mounted on either end of the chamber when one source is not in use, to provide axially-aligned view of the entire helicon or cathode plasma cross section.

Significant effort is required to obtain measurements with good signal to noise ratio (SNR) with the helicon RF source. The helicon antenna and impedance matching network capacitors are contained in a copper mesh Faraday cage with gasket door. A low inductance ground plane that runs under the entire length of the machine and the RF amplifier is provided by a 0.76 mm thick × 91 cm wide copper sheet (cf Fig. 1). The machine legs and RF amplifier chassis are soldered to this ground plane through multiple low inductance connections (10 cm wide copper strips). All probes use coaxial cable with grounded outer conductor (insulated from metal probe shafts) running from close to the probe tip (∼ few cm or less) to the coaxial vacuum feed through. While this adds significant capacitance to the probe load and can add measurement complexity, especially for high frequency measurements of high impedance sources (e.g. fluctuating floating potential, V_f), it has been found to be necessary in order to reduce RF pickup to acceptable levels. Where possible, low pass filtering is used at the output of external cables from probe shaft outputs (i.e. for low frequency measurements). All measurement electronics are contained in grounded boxes or Faraday cages. Metal probe shafts entering the chamber are left floating, but are 'AC grounded' by connecting one or more RF capacitors between the probe shaft and grounded chamber near the vacuum feed through points. All instrumentation connected to the chamber (e.g. vacuum gauges, automated valves, turbo pump) receive power from a common equipment rack which is isolated from building power ground by an isolation transformer.

A relatively extensive set of diagnostics is available on HelCat, including electrostatic and magnetic (B-dot loop) probes, millimeter wave interferometry, visible spectroscopy, fast photodiodes, and fast visible imaging. A LIF system based on a 500 mW tunable diode laser centered at 696 nm, suitable for neutral Ar density, temperature and flow measurements is currently being developed. This system will use 696.543 nm light to probe the $(2P^0_{3/2})4s^2$ neutral metastable state, and fluorescence will be observed at 772.42 nm, as described by Bieber et al. (2013). A number of different types of electrostatic probes are routinely operated, including single and double Langmuir probes (Chen 1965), triple probes (Hershkowitz 1989), Mach probes (MacLatchy et al. 1992), and flux probes (Tsui et al. 1992). Typically, cylindrical probes are utilized. When probes are swept, RF compensation is utilized (Sudit and Chen 1994), but probes collecting ion saturation current, I_{is}, or V_f are left uncompensated. A 94 GHz interferometer is located near the helicon source end, while a 40 GHz interferometer is located closer to the cathode source. Both systems are homodyne quadrature, and utilize Gaussian beam optics. Visible survey spectroscopy over the range $\sim 300 - 800$ nm is provided by a McPherson 205f, 0.5 m, f/3.2 imaging spectrometer. A McPherson 2062DP 4 m spectrometer is used for high resolution visible spectroscopy. This system can, for example, provide Doppler

https://doi.org/10.1017/S0022377814000919 Published online by Cambridge University Press

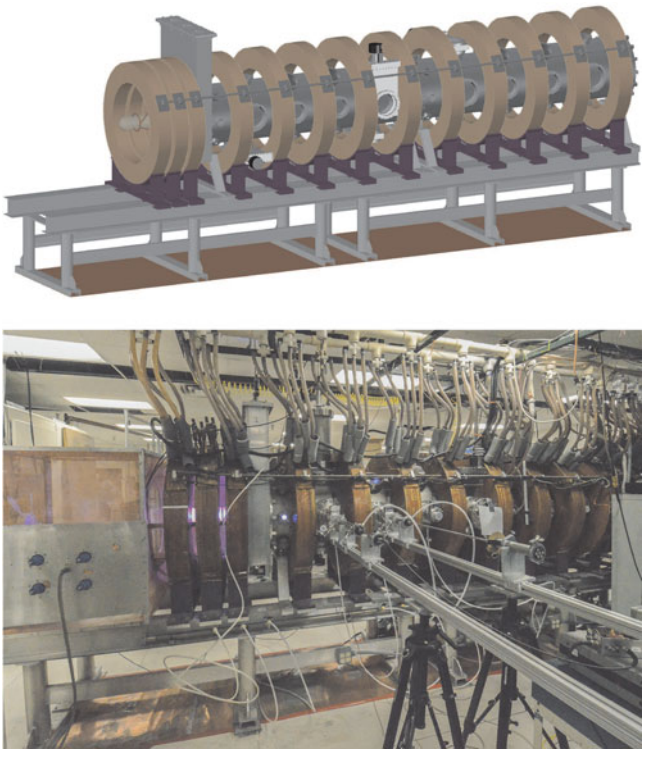


FIGURE 1. HelCat device. Upper: CAD drawing shows helicon source Pyrex tube and helical antenna on chamber south end (left). Large port box can be seen near helicon source, and machine sits on a copper sheet ground plane, as shown. Not shown: cathode source on north end (right) and helicon matching network and Faraday cage. Lower: HelCat photo (helicon matching network and Faraday cage shown on left).

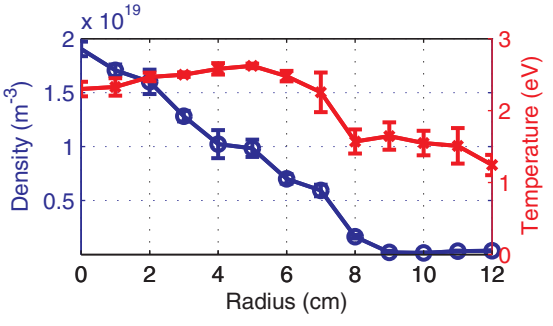


FIGURE 2. Typical HelCat helicon time-average plasma density, n, and electron temperature, T_e, radial profiles. Argon plasma, $B_0 = 0.035$ T, $p_0 = 0.32$ Pa, RF source power $P_{RF} = 1600$ W.

ion temperature measurements with a lower limit of $T_i \sim 7$ eV. A Vision Research Phantom V7.3 camera provides video imaging at up to 500 000 frames/sec, and a Stanford Computer Optics 4 Quick/E provides single frame images at exposure times $\geqslant 1.2$ ns.

https://doi.org/10.1017/S0022377814000919 Published online by Cambridge University Press

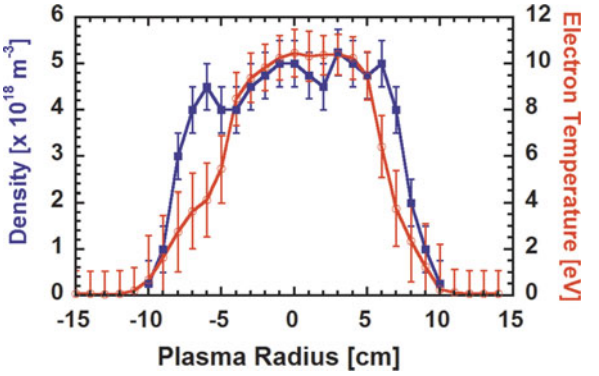


FIGURE 3. Typical HelCat cathode time-average plasma density, n, and electron temperature, T_e, radial profiles. Argon plasma, $B_0 = 0.035$ T, $p_0 = 0.09$ Pa, discharge (emission) current, $I_{dis} = 450$ A.

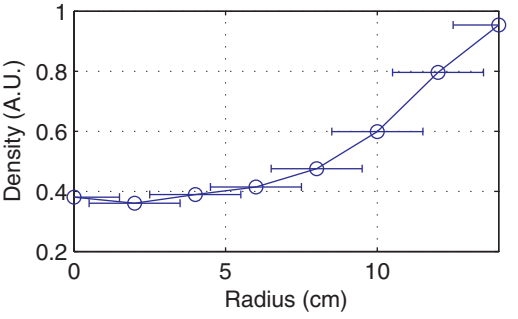


FIGURE 4. Relative neutral Ar density, n_n , versus radius estimated from passive spectroscopic measurements in HelCat. Values are derived from average intensity of four ArI lines, I_{ArI}, (738.5 nm, 750.5 nm,, 794.9 nm, and 811.6 nm) divided by the square root of the average intensity of four ArII lines, $\sqrt{I_{ArII}}$, (434.8 nm, 441.9 nm, 480.6 nm, and 487.9 nm). $I_{ArI}/\sqrt{I_{ArII}}$. $B_0 = 0.035$ T, $p_0 = 0.32$ Pa, RF source power $P_{RF} = 1600$ W.

3. Current and ongoing experiments

3.1. *Fundamental studies of electrostatic turbulence and transport*

Experiments on electrostatic turbulence and transport dynamics in the presence of sheared flows are ongoing in HelCat. In particular, recent experiments in HelCat have focused on understanding fluctuation and transport dynamics in the presence of sheared flows controlled by biased electrode-induced $E_r \times B_{0z}$ flow. We use *control* neither in the engineering sense of a feedback control system, nor in the sense of being able to set a desired flow profile by controlling bias levels on electrodes. Here we use *control* simply to mean *affect*, in the sense that electrode biasing can strongly affect azimuthal and axial plasma flow profiles. We emphasize that when electrode biasing is applied, the plasma generates its own nonlinear response, and that inducing arbitrary flow profiles has not been possible. Nevertheless, biasing is a powerful tool for modifying 'intrinsic' flow profiles and studying the resulting changes to fluctuation and transport dynamics. Additionally, when high positive electrode biasing is applied, such that a strong electron sheath is present, a large amplitude, global instability, identified as a potential relaxation instability (PRI) (Iizuka et al. 1982) is observed. Detailed manuscripts discussing our recent results are currently in preparation and

https://doi.org/10.1017/S0022377814000919 Published online by Cambridge University Press

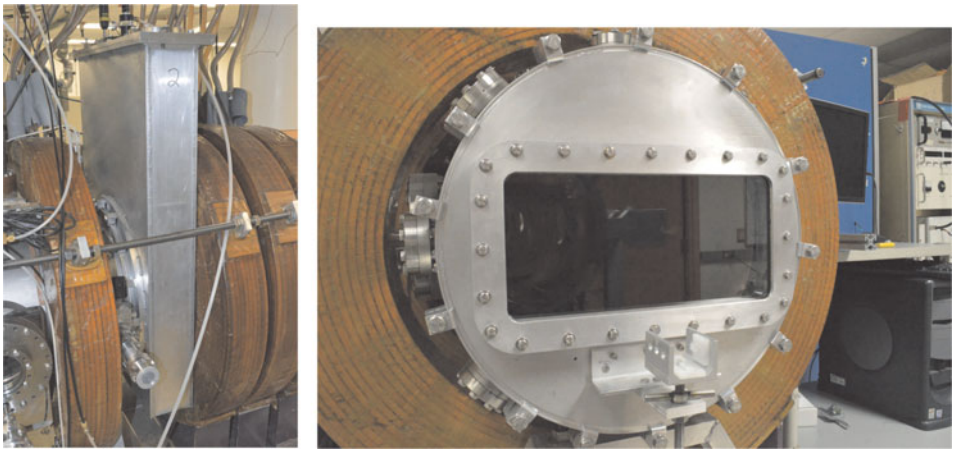


FIGURE 5. Left: Box port. Right: End window (20 × 40 cm) with axial view of full plasma cross section.

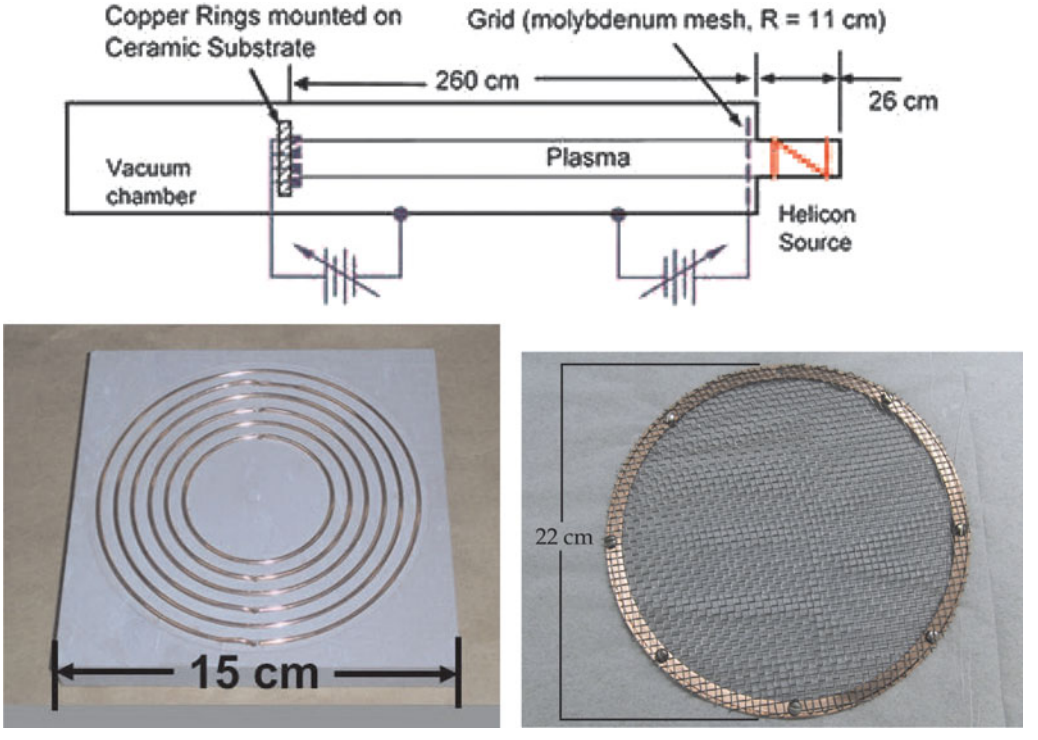


FIGURE 6. Upper: ring and grid biasing arrangement. Lower left: concentric bias rings. Rings are copper, mounted on a 15 cm diameter ceramic substrate. Lower right: Mo grid electrode, diameter: 22 cm. Kepco BOP power op amps are used to drive the rings and grid.

will be published elsewhere (Desjardins and Gilmore 2014; Desjardins et al. 2014). Here, an overview of recent results from the helicon source is presented.

Figure 6 shows the two basic biasing schemes used to date in HelCat: (1) a set of concentric metal rings mounted on an insulating substrate that terminate the plasma

https://doi.org/10.1017/S0022377814000919 Published online by Cambridge University Press

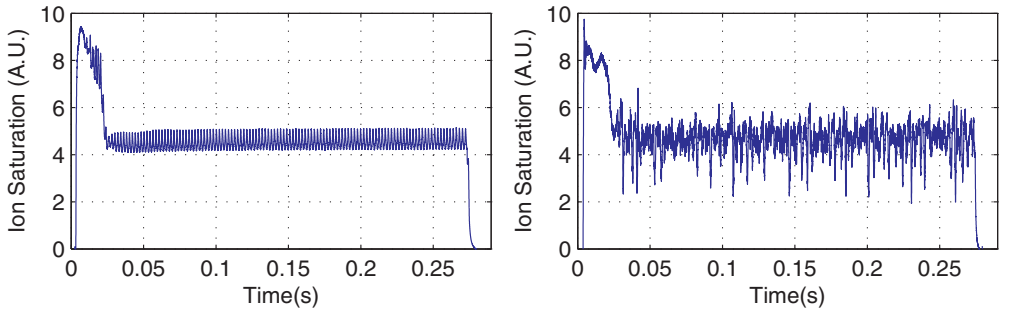


FIGURE 7. Ion saturation current, I_{is}, versus time at $B0 = 0.035$ T (left) and 0.15 T (right) over the entire 270 ms discharge at $r = 6$ cm. Between 0 and 25 ms high RF power is applied for efficient breakdown, then reduced to a steady state level. Argon plasma, $p_0 = 0.32$ Pa, $P_{RF} = 1600$ W (steady state). No electrode bias.

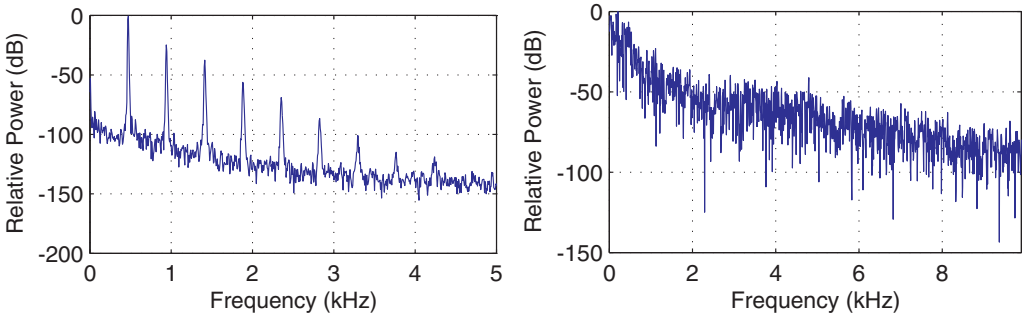


FIGURE 8. Ion saturation current, I_{is}, power spectra at $B_0 = 0.035$ T (left) and 0.15 T (right) at $r = 6$ cm. Argon plasma, $p_0 = 0.32$ Pa, $P_{RF} = 1600$ W. No electrode bias.

column, and (2) a semi-transparent grid (mesh) electrode(s) mounted just in front of the helicon source. Figures 7 and 8 show typical time traces and power spectra of ion saturation current, I_{is}, at $B_0 = 0.035$ T and 0.15 T, respectively, when no biasing electrodes are present. Figure 9 plots a typical example of the RMS amplitude of I_{is} fluctuations versus plasma radius. It can be seen that, as is typical, fluctuations are predominantly coherent at low B-field and more broadband (turbulent) at higher field. However, the spectral details of the fluctuations depend strongly on RF source power and fill pressure.

At low magnetic fields, experiments indicate that 'intrinsic' fluctuations (i.e. without electrode biasing) are consistent with resistive drift waves driven by the radial density gradient. In coherent cases, the axial wavenumber, $k_\parallel$, is finite, with $k_\parallel = 2\pi/\lambda_\parallel \approx 2\pi/2L = \pi/L$, where L is the machine length. Propagation is in the electron diamagnetic direction (EDD), with azimuthal mode number $m = 1, 2,$ or 3, typically, depending on parameters (B-field, RF power, gas fill pressure). $m = 1$ is most often observed. Beta is typically $\sim 10^{-4}$. Axial wavenumber and azimuthal mode number are both measured using the standard two-point probe technique with axially or azimuthally displaced pairs of probes, respectively (Ritz et al. 1988). The normalized density fluctuation level, $\tilde{n}/n$, to potential fluctuation level, $\tilde{\phi}$, scaling expected for drift waves (Jassby 1972), $\tilde{n}/n \sim e\tilde{\phi}/T_e$, is observed, and the cross phase is found to be $\sim$20–30°, typically. $\tilde{n}$ is derived from $\tilde{I}_{is}$ and $\tilde{\phi}$ is derived from floating potential fluctuation measurements, $\tilde{V}_f$, both assuming that T_e fluctuations

https://doi.org/10.1017/S0022377814000919 Published online by Cambridge University Press

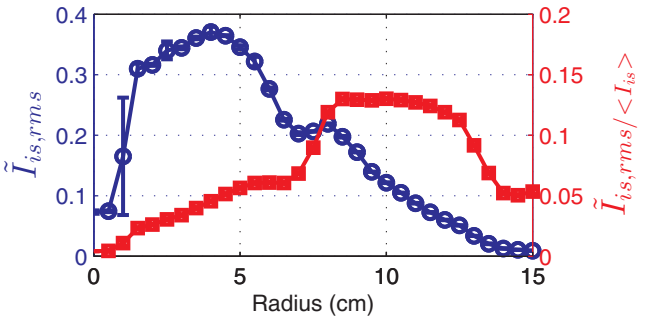


FIGURE 9. RMS amplitude of fluctuating ion saturation current, $\tilde{I}_{is,rms}$ [A.U.], and normalized $\tilde{I}_{is,rms}/\langle I_{is}\rangle$ versus radius during steady state. Argon plasma, $B_0 = 0.035$ T, $p_0 = 0.32$ Pa, $P_{RF} = 1600$ W. No electrode bias. Note that error bars are plotted on every point, but most are small.

are negligible. Observed real frequencies, $f = \omega/2\pi$, of the lowest order modes are typically <1 kHz. For comparison, a rough estimate of expected drift wave frequencies can be made from the analytical expression (Jassby 1972) $\omega \approx \omega^* \pm \omega_{E\times B}$, where ω^* is the diamagnetic frequency and $\omega_{E\times B}$ is the $E \times B$ frequency. These are given by

$$\omega^* = k_\theta \frac{T_e}{eB_0}\frac{1}{n}\frac{dn}{dr} = \frac{m}{r}\frac{T_e}{eB_0}\frac{1}{L_{nr}} \tag{3.1}$$

and

$$\begin{aligned}\omega_{E\times B} = k_\theta v_{\theta,E\times B} &= \frac{m}{r}\left(1 + \frac{\rho_i^2}{4}\nabla^2\right)\frac{\boldsymbol{E}\times\boldsymbol{B}}{B_0^2} \\ &= \frac{m}{rB_0}\left[E_r\left(1 - \frac{1}{r^2}\right) + \frac{\rho_i^2}{4}\left(\frac{\partial^2 E_r}{\partial r^2} + \frac{1}{r}\frac{\partial E_r}{\partial r}\right)\right],\end{aligned} \tag{3.2}$$

where r is the mode radius, and E_r is the radial electric field. Here the finite Larmor radius (FLR) correction in cylindrical coordinates has been applied to the usual $E\times B$ velocity (Chen 2006). This has been found to be necessary since radial gradients of E_r on scales as small as $(2-3)\rho_i$ are routinely measured, and estimates using $v_{E\times B} = E_r/B$ often give non-physical supersonic velocities. We note that Reynolds et al. (2006) have also reported flow velocities measured by LIF significantly less than $v_{E\times B} = E_r/B$ in a Q-machine with radial E_r gradients on the order of ρ_i. We also note that in HelCat, the lack of a T_i measurement makes it difficult to accurately determine ρ_i, and therefore $\omega_{E\times B}$, via plasma potential measurements. Taking $m = 1$, $r = 6.5$ cm, $L_{nr} = 9$ cm, $T_e = 3$ eV, and $B = 0.035$ T gives $f^* = \omega^*/2\pi \approx 2.3$ kHz. This estimate suggests that the mode is strongly Doppler downshifted (d.s) by a flow in the ion diamagnetic direction (IDD) with $f_{d.s.} = \omega_{d.s.}/2\pi \approx 1.6$ kHz. This would correspond to an azimuthal flow in the IDD direction of $v_\theta = 2\pi r f_{d.s.} \approx 650$ m/s $\approx 0.2c_s$, which is within the typical range measured by Mach probes.

In addition to experimental observations, interpretation of the nature of the observed fluctuations is assisted by the use of a linear eigenmode solver code, LSS (Linear Stability Solver), which solves the drift reduced Braginskii equations in the electrostatic limit (Rogers and Ricci 2010). The code takes as input experimental profiles of n, Φ_p, T_e and $k_\parallel$, and calculates the radial eigenfunction, real frequency, ω, and growth rate, γ, for each azimuthal mode number m. It does not calculate a saturated state (i.e. it is a linear code) or a fluctuation spectrum. Inherent in this

https://doi.org/10.1017/S0022377814000919 Published online by Cambridge University Press

solver are resistive drift (DW), ideal rotation-driven interchange (II), resistive rotation-driven interchange (RI), and azimuthal velocity shear-driven Kelvin–Helmholtz (KH) modes. Note that the II and KH modes are most unstable for $k_\parallel \to 0$ (i.e. finite $k_\parallel$ is stabilizing), while the RI and DW modes have $k_\parallel \neq 0$ (Ricci and Rogers 2009). By exploring with the code how parameters such as radial profiles of density and potential affect growth rates and real frequencies at values of m and $k_\parallel$ observed in the experiment, one can obtain a picture of what instability drive (or drives) is at work. Results of analysis with LSS for unbiased helicon plasmas, indicate that the predominant instability drive is density gradient rather than potential gradient (rotation), propagation is in the EDD, and $k_\parallel$ is non-zero. This strongly suggest that unstable modes are consistent with resistive drift waves. Additionally, fully nonlinear, global simulations of HelCat helicon plasmas are now being performed by collaborators at Dartmouth College using the GBS code (Rogers and Ricci 2010).

As parameters are varied in the experiment, especially B-field, and when electrode biasing is applied, other modes are observed. In particular a core ($r \lesssim 4$ cm) mode, which may be consistent with RI, is observed at intermediate B-fields (e.g. 0.065 T $\lesssim B_0 \lesssim$ 0.085 T), and an edge ($r \gtrsim 8$ cm) mode consistent with KH is observed in some cases of high electrode bias. More than one mode (DW, RI, KH) may be present simultaneously, and may be intermittent. Again, details will be presented elsewhere.

When concentric rings (or a solid metal plate) terminate the plasma column and are grounded to the chamber wall, or are left floating, plasma profiles and fluctuations remain nearly unchanged. In fact, end boundary conditions are observed to have little effect on the plasma until significant electron current is drawn at the end. Solid metal plates or meshes, either grounded or floating, placed $z \geqslant 2.5$ m downstream from the source, on the grounded chamber end at $z = 4$ m, or on the large insulating window at $z = 4$ m (cf. Fig. 5) all appear to yield the same plasma profile and fluctuation behavior. This appears to be fundamentally different to end effects reported in the CSDX experiment, where end boundary conditions result in significant differences (Burin et al. 2005). We speculate that the difference is due to HelCat's longer length – HelCat helicon plasmas may effectively terminate on a resistive neutral gas layer rather than a Bohm sheath at the solid surface.

Additionally, when an end electrode is biased negatively with respect to (w.r.t.) the chamber wall, no effects on the plasma are observed. However, when end electrodes are biased positively, strong effects on the character and dynamics of the fluctuations can occur. An example is shown in Fig. 10, where ring electrodes are pulsed on to different voltages at two times during the discharge. Current drawn to the rings with $V_{bias} > \sim 3T_e$ is consistent with electron saturation current levels, $I_{es} = Aj_{es} = A\frac{env_{the}}{4}$, where A is the ring surface area. In Fig. 10 it can be seen that at $V_{bias} \sim 5T_e$ the fluctuation amplitude reduces during the pulse. At $V_{bias} \sim 7T_e$, the fluctuation amplitude is fully suppressed (the RMS amplitude is reduced by > 35 dB). At higher B-field, higher RF power, or different gas fill pressure, fluctuation suppression with ring biasing remains qualitatively unchanged, but the quantitative details of bias levels vary. In general, it is more difficult (i.e. higher bias voltage required) to suppress at high B_0 or P_{RF}. Biasing with the grid electrode just in front of the helicon source produces qualitatively the same behavior as with the rings, but also with quantitative differences.

Figure 11 plots a spectrogram of fluctuations near the edge as the ring bias, V_{bias}, is increased at low magnetic field where fluctuations are relatively coherent. It can be seen that there is a downshifting of the fundamental mode ($f \approx 600$ Hz at zero bias) and other harmonics as bias is increased, consistent with a Doppler downshift due

https://doi.org/10.1017/S0022377814000919 Published online by Cambridge University Press

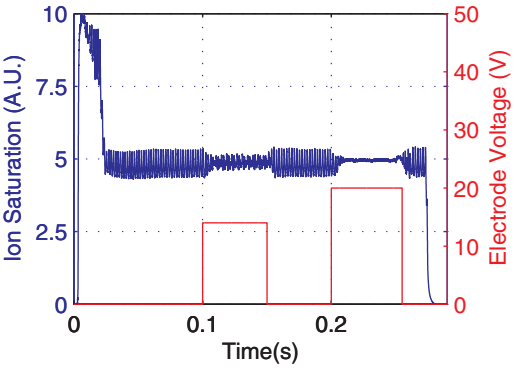


FIGURE 10. Ion saturation current versus time at $r = 6$ cm with pulsed ring biasing. All rings connected together and biased w.r.t. the chamber wall. Argon plasma, $B_0 = 0.035$ T, $p_0 = 0.32$ Pa, $P_{RF} = 1600$ W.

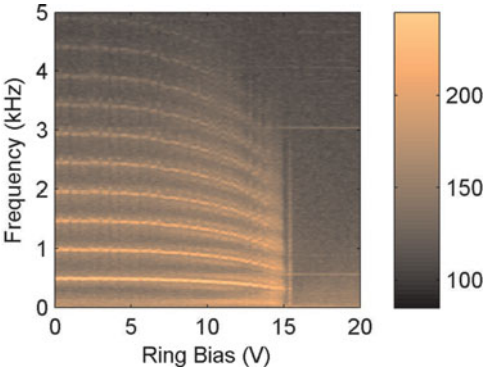


FIGURE 11. Spectrogram of ion saturation current versus ring bias voltage at $r = 6$ cm. Fluctuation suppression occurs at $V \approx 15$ V. All rings connected together and biased w.r.t. the chamber wall. Argon plasma, $B_0 = 0.035$ T, $p_0 = 0.32$ Pa, $P_{RF} = 1600$ W.

to increased $E \times B$ rotation in the IDD. At $V \approx 15$ V, fluctuations are suppressed after going through a change in dynamics (broadband 'strip' at just over 15 V). Just before suppression, chaotic fluctuations are often observed, as will be described in detail elsewhere (Desjardins et al. 2014).

Figure 12 shows the radial electric field, derived from plasma potential measurements using a swept probe as the bias voltage on the end rings is varied. It can be seen that, as is typical, the radial E_r gradient increases in the plasma edge with increasing ring bias. Mach probes also indicate that both axial and azimuthal velocity shear, $\partial V_\theta/\partial r$ and $\partial V_z/\partial z$, respectively, increase with V_{bias}. As mentioned above, azimuthal flow speeds derived simply from $v_\theta = E_r \times B_0$ give unphysical supersonic flow speeds, and estimates using the FLR correction (3.2) have a large amount of error. Thus, quantitative comparisons of velocity shearing rates, $\omega'_{E\times B}$, to linear DW growth rates (measured or calculated), or more exact theory comparisons using $\omega'_{E\times B}$ (e.g. Ware et al. (1998); Terry (2000)) have so far yielded ambiguous results. We should also note that, since the drift wave mechanism acts to balance parallel electron currents via perpendicular ion polarization currents, changes in E_r would automatically be expected to affect linear drift wave dynamics. This work to understand the drift wave dynamics relation to E_r and E_r shear is ongoing.

https://doi.org/10.1017/S0022377814000919 Published online by Cambridge University Press

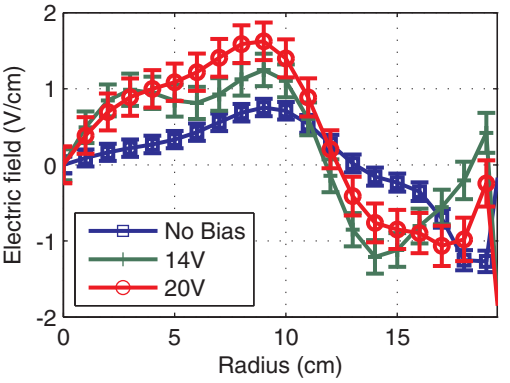


FIGURE 12. Radial electric field versus radius for several ring bias voltages. All rings connected together and biased w.r.t. the chamber wall. Argon plasma, $B_0 = 0.035$ T, $p_0 = 0.32$ Pa, $P_{RF} = 1600$ W.

'Parallel' biasing between a grid near the source and end rings has also been performed, with both electrodes floating w.r.t. the chamber wall (ground). As bias voltage varies, it is found that a Langmuir probe I-V characteristic current flows through the plasma between the electrodes. When $V_{bias} \gtrsim \Phi_p$, electron saturation current flows to the more positive electrode. In such cases, no fluctuation suppression has been observed, despite the fact that the same levels of current are drawn from the plasma as in the 'radial' biasing cases (biasing w.r.t. the wall). This strongly suggests that suppression is most directly associated with radial electric field, rather than parallel current, $j_\parallel$, and a short circuiting of the axial E-field. Of course, $j_\parallel$ and E_r are not independent (i.e. they evolve self-consistently), but it appears that the suppression physics is most directly tied to E_r.

At very high levels of grid bias, e.g. $V_{grid} \gtrsim (10-15)T_e$ (depending on parameters B_0, P_{RF}, etc), where a strong electron sheath is present at the grid, a new, large amplitude mode is observed. This is shown in Fig. 13 where ion saturation current is plotted with a high voltage pulsed grid bias being applied between 0.1–0.2 s. This mode has large amplitude density and potential fluctuations, e.g. $\tilde{n}/n \sim 0.5$–1.0, and propagates axially. The frequency is low, $f \sim$65–135 Hz $\sim 10L/c_s$, where L is the plasma axial length. It is also global, meaning density and potential fluctuations occur in-phase across the entire plasma radius. Upstream of the grid (toward the source), high density regions propagate supersonically at $v \sim 2c_s$. Downstream from the grid, they propagate at $v \sim v_{thi}$ (from an estimated T_i). We have identified this mode as a PRI (Iizuka et al. 1982), which is sometimes referred to as a moving double layer (Iizuka et al. 1982). At moderate biases, e.g. $V_{grid} \gtrsim$ (7–10) T_e the PRI can be intermittent. In such cases, an edge mode, consistent with KH, is sometimes observed growing up during times when the PRI is inactive. When the PRI turns on, this edge mode then disappears.

The PRI has been observed previously in low density glow discharges (Fujita et al. 1987; Gyergyekt et al. 1994) and Q-machines (Iizuka et al. 1982), but, to our knowledge, this is the first observation of the PRI in a high density plasma, such as a helicon. The PRI is a purely nonlinear phenomenon (Fujita et al. 1987), so a linear analytical theory does not appear to exist. Reported scalings of the PRI, for example mode frequency scaling with density, have been purely empirically derived, and it is not known if such scalings apply to densities as high as those of a helicon plasma.

https://doi.org/10.1017/S0022377814000919 Published online by Cambridge University Press

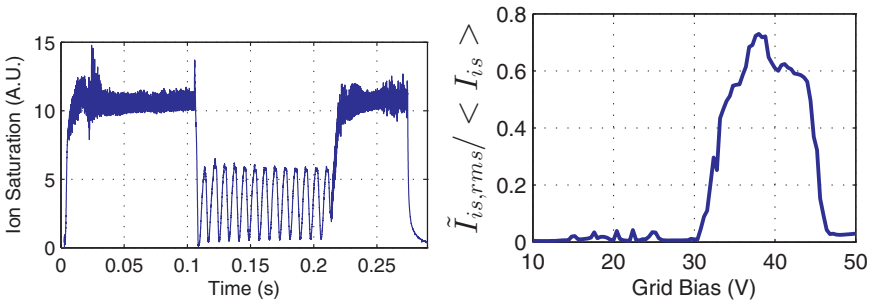


FIGURE 13. Left: ion saturation current, I_{is}, versus time with a large grid bias pulse, $V_{grid} \sim 13T_e$. Right: RMS amplitude of $\tilde{I}_{is}$ versus grid bias. PRI turns on at approximately 30 V. At very high bias the entire discharge collapses. Argon plasma, $B_0 = 0.044$ T, $p_0 = 0.32$ Pa, $P_{RF} = 1600$ W.

Detailed work on the PRI in HelCat will be reported in a forthcoming manuscript (Desjardins and Gilmore 2014).

3.2. *Magnetic relaxation in a background plasma and magnetic field*

One of the experiments currently operating on the HelCat facility involves the study of magnetized plasma bubbles or jets formed and injected radially into the HelCat vacuum vessel by a coaxial plasma gun. The first coaxial plasma gun experiments were performed over 50 years ago by Alfvén, Lindberg, and Mitild (Alfvén et al. 1960), where plasma generated by an early form of coaxial gun was found to exhibit interesting helical features and flux amplification. More recent experiments have examined the behavior of plasma bubbles injected into a vacuum (Yee and Bellan 2000; Hsu and Bellan 2005). However, outside of a small amount of work related to tokamak fueling (Brown and Bellan 1990a,b), little work has been done to study in detail the interaction physics of a coaxial gun plasma with another plasma.

The primary objective of the HelCat coaxial gun experiments is to investigate in a laboratory plasma setting how a magnetized, higher density and pressure plasma ('bubble') relaxes as it propagates into a lower density and pressure plasma ('background') (Liu et al. 2008*a*). This study is motivated by proposed models of extra-galactic radio lobes which are thought to be gigantic relaxed plasmas with kilo-to-megaparsec length galactic jets, providing a source of magnetic energy and helicity (Kronberg et al. 2001; Liu et al. 2008*b*). This topic (bubble propagation through background plasma) is also relevant to core fueling applications in fusion plasmas (Liu et al. 2009).

These plasma bubbles are formed by a compact coaxial gun (Zhang et al. 2009) with ~100 kA current driven by a 120 μF 10 kV capacitor bank (gun bank) as shown schematically in Fig. 14. Various gases such as argon and helium can be puffed into the bore of the gun (between the inner and outer electrodes; see Fig. 15) where an ignitron switched current discharge from the gun bank breaks down the gas. The now ionized gas is then driven out of the gun and into the vacuum vessel by $\boldsymbol{J} \times \boldsymbol{B}$ forces. A bias magnetic field with up to 3 mWb of magnetic flux is embedded in the gun plasma by current in an external solenoid coil driven by a 60 mF 250–450 V capacitor bank.

An overview layout of the coaxial gun is shown in Fig. 15. A typical discharge lasts ~100 μs, during which the gun current undergoes several oscillations. The system acts as an underdamped circuit. We typically only concern ourselves with the first plasma bubble that is formed and ejected. However, in certain cases a second bubble

https://doi.org/10.1017/S0022377814000919 Published online by Cambridge University Press

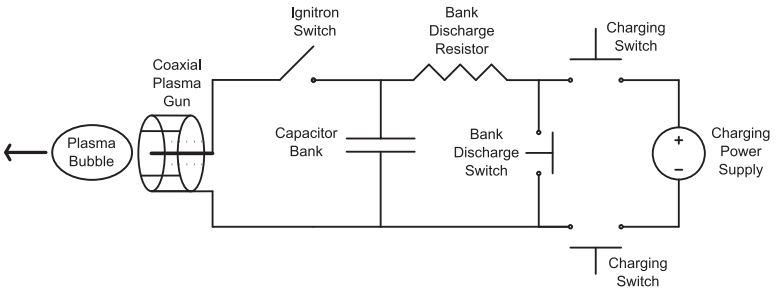


FIGURE 14. The electrical circuit of the coaxial plasma gun.

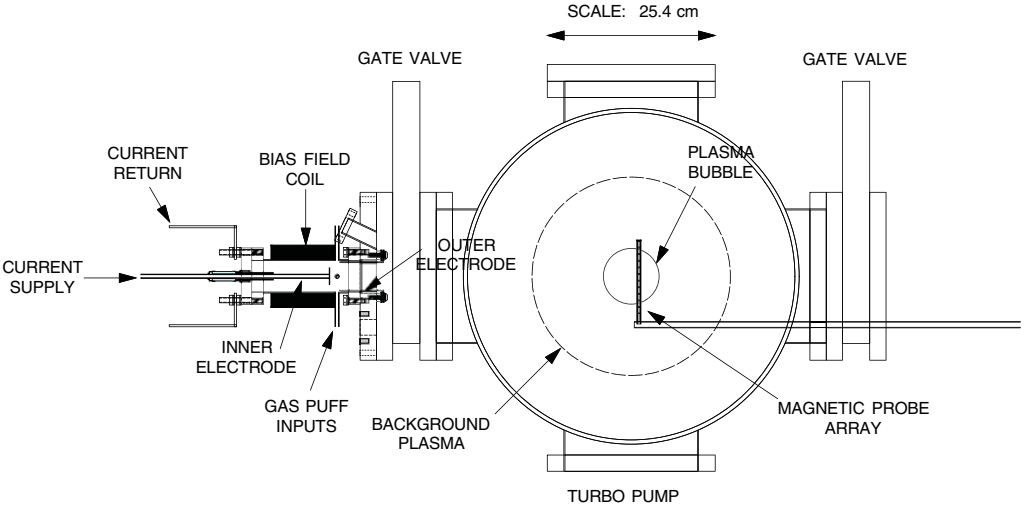


FIGURE 15. Cross-section view of coaxial plasma gun and magnetic probe on the HelCat vacuum chamber.

is formed and can catch up to the first bubble (see Fig. 16 for example). This can allow us to observe the interaction between separate bubbles as they collide, with or without the additional presence of a background plasma.

The main focus of research is bubble interaction with the HelCat background plasma (see Sec. 2). The background plasma species (typically argon or helium) can be the same or different than the gun plasma species. This gives us the flexibility to investigate physical effects depending on charge state and/or ion mass. The background can also be expanded in radius by flaring the background B-field in HelCat. This allows the size of the background plasma relative to the bubble plasma to be varied. Typical plasma parameters for the plasma bubbles are $n_e \sim 10^{20}$ m^{-3}, $T_e \sim 5 - 10$ eV, $T_i \sim 10 - 15$ eV. Plasma densities were measured by Langmuir probes biased into ion saturation, ion temperatures were determined from Doppler line broadening, and electron temperature was determined by electrostatic triple probe measurements. Visible camera imaging did not indicate any significant perturbation, such as impurity generation, due to the probes. Propagation velocities are $\sim 5 \times 10^3$ m/s (argon) and $\sim 15 \times 10^3$ m/s (helium), which are roughly the corresponding ion sound speeds for each plasma.

https://doi.org/10.1017/S0022377814000919 Published online by Cambridge University Press

A key parameter of the gun plasma is λ_{gun} which is given by Hsu and Bellan (2005) as

$$\lambda_{gun} \equiv \mu_o \frac{I_{gun}}{\Phi_{B,gun}}, \tag{3.3}$$

where I_{gun} is current in amps flowing through the gun plasma, and $\Phi_{B,gun}$ magnetic flux in Webers linking the inner and outer electrodes. It is well established in coaxial gun spheromak experiments (Geddess et al. 1998; Yee and Bellan 2000) that if the parameter $\lambda_{gun} \gtrsim 3.8/r_{gun}$ (where r_{gun} is the gun radius from inner to outer electrode) then a spheromak 'bubble' will be formed by the discharge. The gun bank voltage controls I_{gun} while the bias bank voltage controls $\Phi_{B,gun}$, allowing λ_{gun} to be varied over a range $\sim 50 - 1500$ in our experiments.

For our coaxial gun, $r_{gun} = 2.4 \times 10^{-2}$ m so $\lambda_{critical} = 3.8/r_{gun} \sim 158$ m^{-1}. For values of $\lambda_{gun} \lesssim \lambda_{critical}$ the bias flux $\Phi_{B,gun}$ dominates the physics, and the gun plasma may in extreme cases not even detach from the gun. The other extreme, $\lambda_{gun} \gtrsim \lambda_{critical}$, results in a 'jet'-like plasma where $\boldsymbol{J} \times \boldsymbol{B}$ forces dominate and magnetic tension due to the bias flux is less important.

We take as the simplest example case a plasma bubble launched into vacuum. Figure 16 shows a sequence of visible light images (i.e. movie) of an example plasma bubble launched into vacuum with $\lambda_{gun} \approx 93$ m^{-1}. For comparison, we show in Fig. 17 a single example of an argon plasma bubble with $\lambda_{gun} \approx 63$ m^{-1} propagating through a background plasma. The background plasma is also argon with magnetic field 0.035 Tesla, oriented perpendicular to the plasma bubble propagation direction. Note in comparison to Fig. 16 which has a plasma bubble with similar $\lambda_{gun} \approx 93$ m^{-1} but no background plasma, the images with background plasma show obvious differences. Systematically exploring and quantifying these differences is a subject of ongoing work.

The B-field evolution as a function of λ_{gun} is an important part of the physics we wish to investigate. The magnetic field can be reconstructed from an 11 element linear array of 3-axis magnetic probes, similar to those described in Romero-Talamás et al. (2004), providing a total of 33 measurements with $\sim$1 cm spatial resolution. The magnetic array can be moved along the radial direction (along the bubble axis of propagation) in HelCat and also rotated about the probe axis (see Fig. 15) for extensive spatial coverage of the bubble along it's propagation through the vacuum or background plasma.

Experiments are currently in progress to begin characterizing bubble formation and interaction with vacuum, vacuum with magnetic field, and magnetized background plasma as a function of λ_{gun} and other parameters. These experiments will provide the initial base of understanding of bubble behavior that will set the stage for more detailed studies going forward.

4. Device modifications

Magnetic topology, including magnetic shear and X-points, is also known to play an important role in electrostatic turbulence and transport (Su et al. 1992). A detailed investigation of magnetic shear and X-points on turbulence and transport dynamics, including in the presence of biased electrodes, is planned in HelCat. To this end, design and installation of two single turn axial coils is underway. These single turn coils will produce an essentially steady state azimuthal magnetic field whose purpose is to affect the zero-order magnetic topology, not the magnetic dynamics. The concept is shown in Fig. 18. Two axial rods, covered with insulators, and carrying sufficient

https://doi.org/10.1017/S0022377814000919 Published online by Cambridge University Press

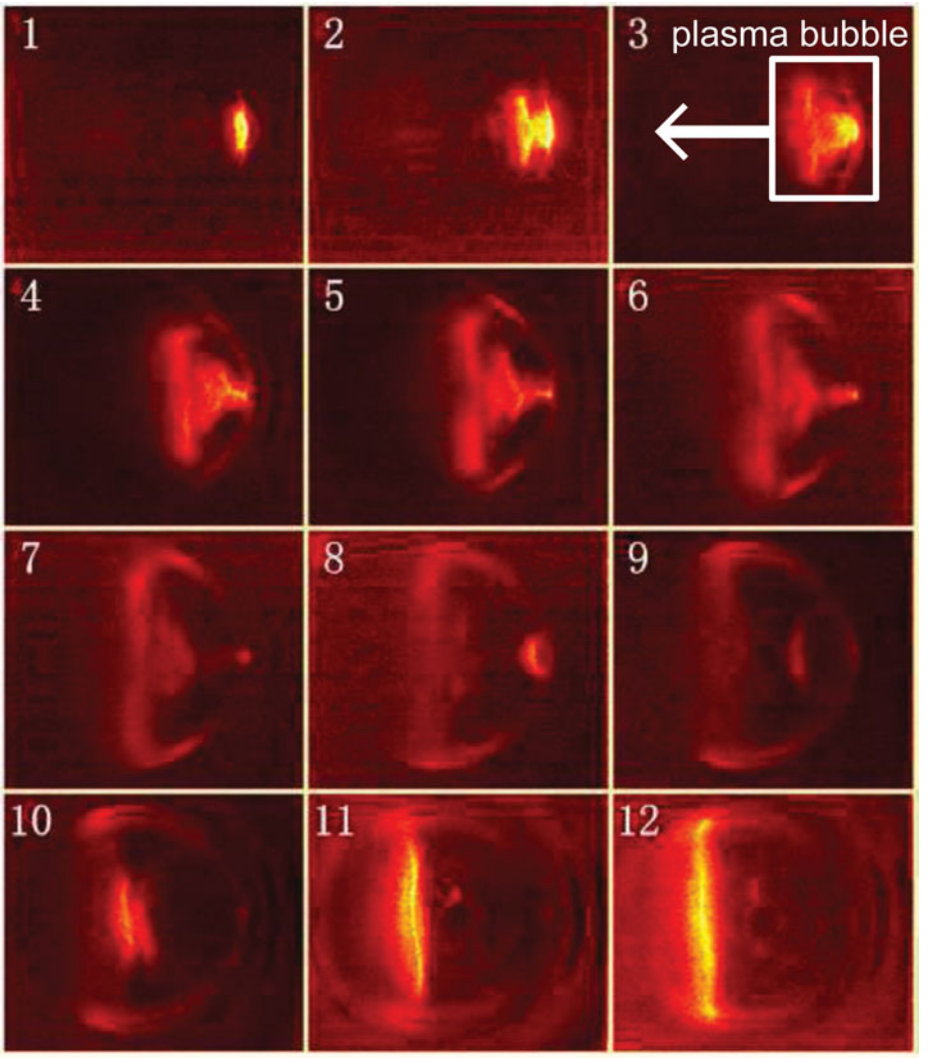


FIGURE 16. Images are ordered in time from 1–12. The frame rate is 4 μs between each frame with exposure time of 1 μs per frame; $\lambda gun \approx 93$ m^{-1}. Plasma (argon) propagates from right to left out of the gun and across the HelCat chamber. Note appearance of a second 'bubble' from the right side of frame 8, which catches up to the first bubble near the center of frame 10. Frames 11–12 show subsequent interaction occurring between the two bubbles, indicated by strong changes in visible light intensity.

current to produce an azimuthal B-field, $B_{\theta 0} \lesssim 0.1$ T at the plasma edge will be installed on axis ($r = 0$) through the helicon source, and off axis at $r = 18$ cm at an existing end port. Required current will be $\leqslant 3.5$ kA, and will be supplied by slow pulse (tens of ms) capacitor banks with solid state switches. Figure 18 also plots the calculated $B_{\theta 0}$ for an example case, showing a magnetic X-point at $r = 7$ cm.

5. Possible future research topics

The HelCat device is located in the same laboratory space as the UNM HPM lab, which is a world leader in short pulse ($\lesssim$100 ns), high power (>100 MW) microwave

https://doi.org/10.1017/S0022377814000919 Published online by Cambridge University Press

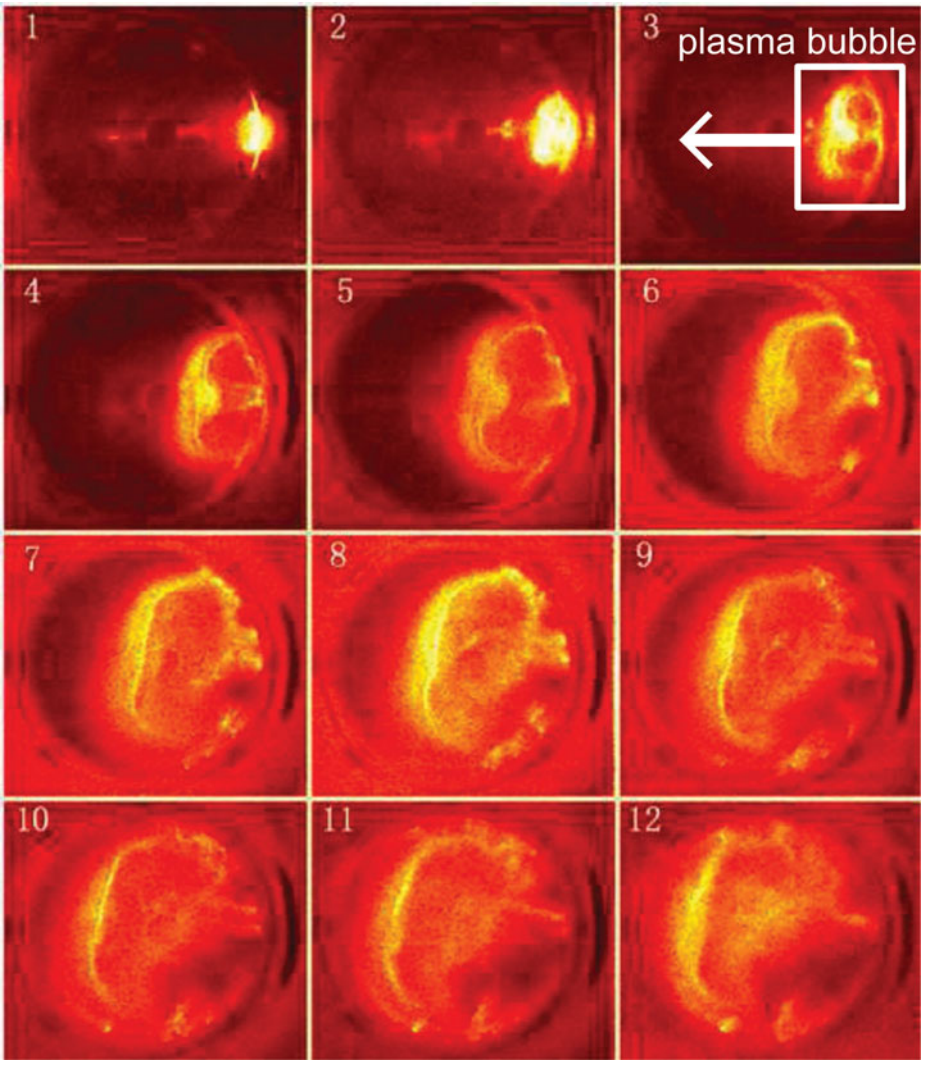


FIGURE 17. Images are ordered in time from 1–12. The frame rate is 2 μs between each frame with exposure time of 1 μs per frame; $\lambda_{gun} \approx 63$ m^{-1}. Plasma bubble (argon) propagates from the right to left out of the gun and through background plasma (argon) with 0.035 Tesla magnetic field (oriented out of the page) in the HelCat chamber.

sources. The area of microwave-plasma interactions is, therefore, a natural line of research in HelCat. The UNM HPM lab has several electron beam accelerators capable of driving HPM sources, including a SINUS-6 accelerator which can deliver a ~15 ns, 600 kV, 1 kA pulse. Several different microwave sources have been driven by the SINUS-6, including an S-band (2.6–3.95 GHz) magnetron with $P > 300$ MW, and an X-band (8.2–12.4 GHz) backward wave oscillator (BWO) with $P > 1$ GW, both for 10 ns (Moreland et al. 1994).

In particular, two HPM-plasma experiments have been proposed, (1) an experiment on RF wakefield acceleration (Kaw and Dawson 1969; Nishida et al. 1994), and (2) an experiment related to electron heating by Langmuir wave turbulence nonlinearly driven by RF heating and parametric decay. For wakefield acceleration,

https://doi.org/10.1017/S0022377814000919 Published online by Cambridge University Press

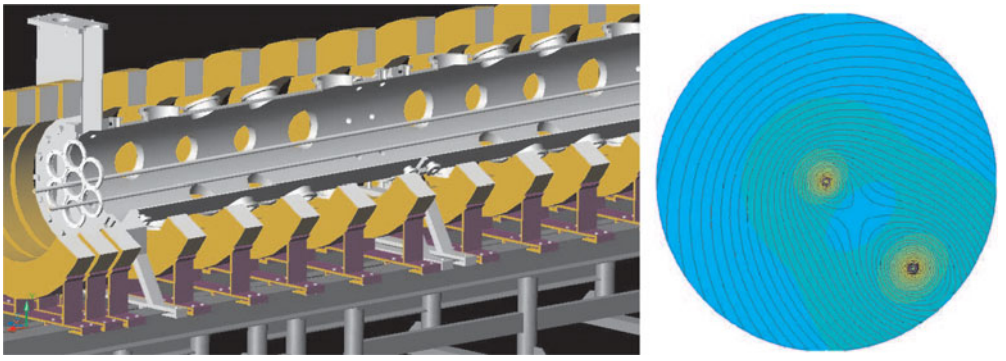


FIGURE 18. Left: Cutaway CAD drawing of HelCat with single turn axial coils added to produce magnetic shear and an X-point. Right: Contours of B_θ calculated in 2D by the FEMM code (FEMM 2014) generated by an on-axis current of 2.5 kA and an off-axis current of 3.5 kA located at $r = 18$ cm. The X-point is located at $r \approx 7$ cm in this case. Nominal plasma size shown in red.

the experiment would be to study the nonlinear interaction of an HPM pulse that is of ns time scale in X-band with an underdense plasma having various spatial density distributions, both with and without a magnetic field. The main goal would be to characterize the effects of the ponderomotive force exerted by the electromagnetic wave field (both by changing the plasma's index of refraction and creating waves in the plasma) by varying the plasma density and the magnetic field. Using the SINUS-6 driven BWO, we have the ability to create conditions that are more than three orders-of-magnitude more intense than those used in previous investigations of wakefield generation using microwave-plasma interactions. The output pulse duration of the source can be adjusted to be $\sim 1/\omega_{pe}$, making the experiment equivalent to traditional laser wakefield acceleration experiments, but in the microwave regime. The HPM pulses need not be as short as the laser pulses, which will allow for simpler, more reliable plasma measurements. This research is relevant to particle acceleration and astrophysics, as well as being a fundamental plasma physics process.

Experiments on electron acceleration by Langmuir turbulence generated by high power RF are motivated by F-layer ionospheric heating experiments where high density plasma was created at altitudes far below the RF deposition region (Pedersen et al. 2010, 2011). A theoretical explanation for this observation has been proposed based on an ionizing wavefront moving downward due to ionization by electrons accelerated by HF-excited plasma turbulence (Mishin and Pedersen 2011). There remains no experimental or observational confirmation of this theory. The HelCat experiment would utilize a few MW of $f_0 = 3$–10 GHz microwave power injected as a Gaussian beam into a spatially inhomogeneous plasma with long density gradient scale length ($L_n \gg \lambda$, the microwave wavelength), and containing the O-mode resonance $f_0 = f_{pe}$. Langmuir turbulence would be measured by an infrared ($\lambda = 10.6$ μm) coherent scattering diagnostic, and possibly microprobes (e.g. Chiang et al. (2011)). Table 3 shows parameters and dimensionless scaled parameters for both the ionospheric (F-reg.) and HelCat experiments. As can be seen, the important dimensionless parameters are well matched.

6. Summary

The HelCat device is a medium-scale basic plasma science experiment that can operate over a relatively wide range of plasma parameters through the use of three

https://doi.org/10.1017/S0022377814000919 Published online by Cambridge University Press

	f_0 (MHz)	f_{pe} (MHz)	f_{ce} (MHz)	T_e (eV)	E_0 (V/m)	$4\nu_e/f_0$	W_A	f_{pe}/f_{ce}
F-reg.	2.8–5	3–6.5	1.3–1.5	0.2–0.3	0.5–2	$(4-8)\times10^{-4}$	0.1–1	2–5
HelCat	$(3-10)\times10^{3}$	$(1-3)\times10^{4}$	$(0.2-6)\times10^{3}$	2–5	$10^{4}-10^{6}$	$(1-40)\times10^{-4}$	0.001–10	1.5–150

TABLE 3. Key plasma and wave parameters for the ionosphere F-region and HelCat.

different plasma sources. It can be reconfigured easily according to the demands of individual experiments, and has a relatively extensive set of diagnostics. A brief description of ongoing experiments on (1) turbulence and transport and (2) magnetic relaxation has been given. Edge fluctuations are found to exhibit a rich variety of dynamics, including chaos and intermittency, as plasma parameters (B_0, P_{RF}, gas fill pressure) are varied and electrode biasing is applied. At moderate electrode bias voltages, fluctuations can be fully suppressed. At high electrode bias levels, e.g. $V_{bias} \gtrsim (10-15)T_e$, a large amplitude, global mode, identified as a PRI is observed. Experiments on the interaction dynamics of a magnetized, higher density and pressure plasma bubble propagating into a lower density and pressure plasma background have been motivated by physics questions around astrophysical jet phenomena. Preliminary studies with fast imaging have shown significant qualitative differences between bubble propagation (with otherwise similar gun parameters) into vacuum versus propagation through a magnetized background plasma. Additionally, two possible future HPM-plasma experiments have been described that leverage HelCat's proximity to unique HPM devices. HelCat is also well suited to a wide range of other fundamental plasma science experiments, such as helicon source physics or nonlinear wave dynamics.

Acknowledgements

The authors would like to acknowledge Paolo Ricci for supplying the LSS code and for many useful discussions and Tyler Wynkoop for assistance with figures. We also thank Glen Wurden of Los Alamos National Laboratory for the loan of the Hadland camera used for Figs 16 and 17. The RF-Langmuir turbulence experiment was suggested by Evgeny Mishen. This work was supported by the US National Science Foundation, the US Department of Energy Office of Science, and the University of New Mexico.

Appendix A. Definition of table variable names

All units are SI (MKS), except temperature in eV.

a – plasma radius
$\boldsymbol{B}$ – magnetic flux density
$c = 3 \times 10^8$ m/s – speed of light in vacuum
$c_s = \sqrt{\kappa(T_e + T_i)/m_i}$ – ion sound speed
$e = 1.6 \times 10^{-19}$ C – electron charge
$L_{nr} = \left(\frac{1}{n}\frac{dn}{dr}\right)^{-1}$ – radial density gradient scale length
$m_e = 9.1 \times 10^{-31}$ kg – electron mass
m_i – ion mass
n – plasma density
n_n – neutral gas density

https://doi.org/10.1017/S0022377814000919 Published online by Cambridge University Press

T_e – electron temperature
T_i – ion temperature
$V_A = B/\sqrt{\mu_o n m_i}$ – Alfvén speed
$\beta = \frac{n\kappa(T_e+T_i)}{B^2/2\mu_o}$ – plasma beta
$\epsilon_o = 8.854 \times 10^{-12}$ F/m – permittivity of free space
$\kappa = 1.6 \times 10^{-19}$ J/eV – Boltzmann constant
$\lambda_D = \sqrt{\frac{\epsilon_o \kappa T_e}{ne^2}}$ – Debye length
$\lambda_{ie} = v_{the}/\nu_{ie}$ – thermal ion-electron collisional mean free path
$\lambda_{ii} = v_{thi}/\nu_{ii}$ – thermal ion-ion collisional mean free path
$\lambda_{in} = \frac{1}{n_n \sigma_{in}}$ – thermal ion-neutral collisional mean free path
μ – ratio of ion mass to proton mass
$\mu_o = 4\pi \times 10^{-7}$ H/m – permeability of free space
$\nu_{ii} = \frac{4.8\times10^{-14} n \ln \Lambda_{ii}}{T_i^{3/2}\mu^{1/2}}$ – thermal ion-ion collision frequency (Huba 2009)
$\nu_{in} = n_n \sigma_{in} v_{thi}$ – ion-neutral collision frequency
$\rho_i = v_{thi}/\omega_{ci}$ – ion gyroradius
$\rho_s = c_s/\omega_{ci}$ – ion sound gyroradius
σ_{in} – total ion-neutral collision cross section
$\omega_{ce} = eB/m_e$ – electron cyclotron frequency
$\omega_{ci} = eB/m_i$ – ion cyclotron frequency
$\ln \Lambda_{ie} = 23 - \ln\left(n^{1/2} T_e^{-3/2}\right)$ – Coulomb logarithm for thermal ion-electron collisions (Huba 2009)
$\ln \Lambda_{ii} = 23 - \ln\left(n^{1/2} T_i^{-3/2}\right)$ – Coulomb logarithm for thermal ion-ion collisions (Huba 2009)

REFERENCES

Alfvén, H., Lindberg, L. and Mitlid, P. 1960 Experiments with plasma rings. *J. Nucl. Energy* C **1**(3), 116.

Bieber, T. Glad, X., de Poucques, L., Hugon, R., Vasseur, J.-L., Bougdira, J. 2013 Argon ion and neutral metastable levels destruction in a magnetically enhanced inductively coupled plasma reactor. *Open Plasma Phys. J.* **6**, 32.

Brown, M. R. and Bellan, P. M. 1990*a* Current drive by spheromak injection into a tokamak. *Phys. Rev. Lett.* **64**(18), 2144.

Brown, M. R. and Bellan, P. M. 1990*b* Spheromak injection into a tokamak. *Phys. Fluids* B **2**(6), 1306.

Burin, M. J., Tynan, G. R., Antar, G. Y., Crocker, N. A. and Holland, C. 2005 On the transition to drift turbulence in a magnetized plasma column. *Phys. Plasmas* **12**, 052 320.

Chen, F. F. 1965 Electric probes. In: *Plasma Diagnostic Techniques,* (ed. R. H. Huddleston and S. L. Leonard). New York: Academic Press.

Chen, F. F. 2006 *Introduction to Plasma Physics and Controlled Fusion*, 2nd edn., Vol. 1. New York: Springer.

Chen, F. F. and Arnush, D. 1997 Generalized theory of helicon waves. I. normal modes. *Phys. Plasmas* **4**(9), 3411.

Chiang, F. C., Pribyl, P., Gekelman, W., Lefebvre, B., Chen, Li-Jen and Judy, J. W. 2011 Microfabricated flexible electrodes for multiaxis sensing in the large plasma device at UCLA. *IEEE Trans. Plasma Sci.* **39**(6), 1507.

Desjardins, T. R. and Gilmore, M. 2014 *Phys. Plasmas* (submitted).

Desjardins, T. R., Gilmore, M., Reynolds-Barredo, J. M. and Fisher, D. 2014 *Phys. Plasmas* (submitted).

https://doi.org/10.1017/S0022377814000919 Published online by Cambridge University Press

Fasoli, A., Labit, B., McGrath, M. et al. 2006 Electrostatic turbulence and transport in a simple magnetized plasma. *Phys. Plasmas* **13**, 055 902.

FEMM 2014 *FEMM Magnetics*, `http://www.femm.info/wiki/HomePage`.

Fujita, H., Yaura, S., Harada, T. and Matsup, H. 1987 Observation of potential relaxation instability in a bounded discharge plasma. *IEEE Trans. Plasma Sci.* **PS-15**(4), 445.

Geddess, C. G. R., Kornack, T. W. and Brown, M. R. 1998 Scaling studies of spheromak formation and equilibrium. *Phys. Plasmas* **5**, 1027.

Gekelman, W., Pfister, H., Lucky, A., Bamber, J., Leneman, D. and Maggs, J. 1991 Design, construction, and properties of the large plasma research device – the LAPD at UCLA. *Rev. Sci. Instrum.* **62**(12), 2875.

Gyergyekt, T., CerEek, M., Stanojevic, M. and Jelids, N. 1994 An investigation of the electrode current oscillations caused by the potential relaxation instability in a weakly magnetized discharge plasma. *J. Phys. D: Appl. Phys.* **27**, 2080.

Hershkowitz, N. 1989 How Langmuir probes work. In: *Plasma Diagnostics: Discharge Parameters and Chemistry,* (ed. O. Auciello and D. L. Falmm). New York: Academic Press.

Hsu, S. C. and Bellan, P. M. 2005 On the jets, kinks, and spheromaks formed by a planar magnetized coaxial gun. *Phys. Plasmas* **12**(3), 032 103.

Huba, J. D. 2009 (2009 revised) NRL Plasma Formulary, `http://www.psfc.mit.edu/library1/catalog/online_pubs/NRL_FORMULARY_09.pdf`.

Iizuka, S., Michelson, P., Ramussen, J. J. and Schrittwiser, R. 1982 Dynamics of a potential barrier formed on the tail of a moving double layer in a collisionless plasma. *Phys. Rev. Lett.* **48**(3), 145.

Jassby, D. L. 1972 Transverse velocity shear instabilities within a magnetically confined plasma. *Phys. Fluids* **15**(9), 1590.

Kaw, P. W. and Dawson, J. M. 1969 Laser-induced anomalous heating of a plasma. *Phys. Fluids* **12**, 2586.

Kronberg, P. P., Dufton, Q. W., Li, H. and Colgate, S. A. 2001 Magnetic energy of the intergalactic medium from galactic black holes. *Astrophys. J.* **560**, 178.

Leneman, D., Gekelman, W. and Maggs, J. 2006 The plasma source of the large plasma device at University of California, Los Angeles. *Rev. Sci. Instrum.* **77**, 015 108.

Light, M. and Chen, F. F. 1995 Helicon wave excitation with helical antennas. *Phys. Plasmas* **2**(4), 1084.

Liu, W., Hsu, S. C. and Li, H. 2009 Ideal magnetohydrodynamic simulations of low beta compact toroid injection into a hot strongly magnetized plasma. *Nucl. Fusion* **49**, 095 008.

Liu, W., Hsu, S. C., Li, H., Li, S. and Lynn, A. G. 2008*a* Ideal magnetohydrodynamic simulation of magnetic bubble expansion as a model for extragalactic radio lobes. *Phys. Plasmas* **15**(7), 072 905.

Liu, W., Li, H., Li, S. and Hsu, S. C. 2008*b* Long-term evolution of magnetized bubbles in galaxy clusters. *Astrophys. J. Lett.* **684**, L57–L60.

Lynn, A. G., Gilmore, M., Watts, C., Herrea, J., Kelly, R., Will, S., Xie, S., Yan, L. and Zhang, Y. 2009 The helcat dual-source plasma device. *Rev. Sci. Instrum.* **80**(10), 103 501.

MacLatchy, C. S., Boucher, C., Poirier, D. A. and Gunn, J. 1992 Gundestrup: a Langmuir/Mach probe array for measuring flows in the scrape-off layer of TdeV. *Rev. Sci. Instrum.* **63**(8), 3923.

Mishin, E. and Pedersen, T. 2011 Ionizing wave via high-power HF acceleration. *Geophys. Res. Lett.* **38**, L01 105.

Moreland, L. D., Schamiloglu, E., Lemke, R. W., Korovin, S. D., Rostov, V. V., Roitman, A. M., Hendricks, K. J. and Spencer, T. A 1994 Efficiency enhancement of high power vacuum bwos using nonuniform slow wave structures. *IEEE Trans. Plasma Sci.* **22**, 554.

Nishida, Y., Kusaka, S. and Yugami, N. 1994 Excitation of wakefield and electron acceleration by short microwave pulse. *Phys. Scr.* **T52**, 65.

Okamoto, A., Hara, K., Nagaoka, K., Yoshimura, S., Vranješ, J., Kono, M. and Tanaka, M. Y. 2003 Experimental observation of a tripolar vortex in a plasma. *Phys. Plasmas* **10**(6), 2211.

Pedersen, T. et al. 2010 Creation of artificial ionospheric layers using high-power HF waves. *Geophys. Res. Lett.* **37**, L02 106.

Pedersen, T. et al. 2011 Production of artificial ionospheric layers by frequency sweeping near the 2nd gyroharmonic. *Annu. Geophys.* **29**, 47.

https://doi.org/10.1017/S0022377814000919 Published online by Cambridge University Press

Reynolds, E. W., Koepke, M. E., Carroll, J. J. and Shinohara, S. 2006 Inhomogeneity scale lengths in a magnetized, low-temperature, collisionless, q-machine plasma column containing perpendicular-velocity shear. *Phys. Plasmas* **13**, 092 106.

Ricci, P. and Rogers, B. N. 2009 Three-dimensional fluid simulations of a simple magnetized toroidal plasma. *Phys. Plasmas* **16**, 092 307.

Ritz, Ch. P. et al. 1988 Advanced plasma fluctuation analysis techniques and their impact on fusion research. *Rev. Sci. Instrum.* **59**(8), 1739.

Rogers, B. N. and Ricci, P. 2010 Low-frequency turbulence in a linear magnetized plasma. *Phys. Rev. Lett.* **104**, 225 002.

Romero-Talamás, C. A., Bellan, P. M. and Hsu, S. C. 2004 Multielement magnetic probe using commercial chip inductors. *Rev. Sci. Instrum.* **75**, 2664.

Scime, E. E., Carr, J., Galante, M., Magee, R. M. and Hardin, R. 2013 Ion heating and short wavelength fluctuations in a helicon plasma source. *Phys. Plasmas* **20**, 032 103.

Su, N. N., Horton, W. and Morrison, P. J. 1992 Drift wave vortices in nonuniform plasmas with sheared magnetic fields. *Phys. Fluids* B **4**(5), 1238.

Sudit, I. D. and Chen, F. F. 1994 RF compensated probes for high-density discharges. *Plasma Sources Sci. Technol.* **3**, 162.

Terry, P. W. 2000 Suppression of turbulence and transport by sheared flow. *Rev. Mod. Phys.* **72**(1), 109.

Tsui, H. Y. W. et al. 1992 A new scheme for Langmuir probe measurement of transport and electron temperature fluctuations. *Rev. Sci. Instrum.* **63**(10), 4608.

Ware, A. S., Terry, P. W., Carreras, B. A. and Diamond, P. H. 1998 Turbulent heat and particle flux response to electric field shear. *Phys. Plasmas* **5**(1), 173.

Watts, C. and Hanna, J. 2004 Alfven wave propagation in a partially ionized plasma. *Phys. Plasmas* **11**(4), 1358.

Yee, J. and Bellan, P. M. 2000 Taylor relaxation and λ decay of unbounded, freely expanding spheromaks. *Phys. Plasmas* **7**, 3625.

Zhang, Y., Lynn, A. G., Hsu, S. C., Gilmore, M. and Watts, C. 2009 Design of a compact coaxial magnetized plasma gun for magnetic bubble expansion experiments. In: *Proc. 17th IEEE Int. Pulsed Power Conf.*, Washington, DC, 28 June –2 July , 2009.

https://doi.org/10.1017/S0022377814000919 Published online by Cambridge University Press